Mechanical
Sciences

Open Access

A two-stage calibration method for industrial robots with joint and drive flexibilities

M. Neubauer[1], **H. Gattringer**[1], **A. Müller**[1], **A. Steinhauser**[1], and **W. Höbarth**[2]

[1]Institute of Robotics, Johannes Kepler University Linz, Altenbergestr. 69, 4040 Linz, Austria
[2]Bernecker + Rainer Industrie Elektronik Ges.m.b.H., B & R Str. 1, 5142 Eggelsberg, Austria

Correspondence to: M. Neubauer (matthias.neubauer_1@jku.at)

Abstract. Dealing with robot calibration the neglection of joint and drive flexibilities limit the achievable positioning accuracy significantly. This problem is addressed in this paper. A two stage procedure is presented where elastic deflections are considered for the calculation of the geometric parameters. In the first stage, the unknown stiffness and damping parameters are identified. To this end the model based transfer functions of the linearized system are fitted to captured frequency responses of the real robot. The real frequency responses are determined by exciting the system with periodic multisine signals in the motor torques. In the second stage, the identified elasticity parameters in combination with the measurements of the motor positions are used to compute the real robot pose. On the basis of the estimated pose the geometric calibration is performed and the error between the estimated end-effector position and the real position measured with an external sensor (laser-tracker) is minimized. In the geometric model, joint offsets, axes misalignment, length errors and gear backlash are considered and identified. Experimental results are presented, where a maximum end-effector error (accuracy) of 0.32 mm and for 90 % of the poses a maximum error of 0.23 mm was determined (Stäubli TX90L).

1 Introduction

One of the main characteristics of industrial robots is their positioning accuracy, strongly depending on the sensor resolution and the geometric parameters. The calculation of the real geometric parameters is called geometric robot calibration and is crucial for accurate robot movements. In literature different calibration methods exist (see Khalil and Dombre, 2004 or Siciliano and Khatib, 2008). However, they are dealing with kinematic models only, neglecting the effects of flexibilities in the joints and drives and thus cause a systematic error in the calculation of the real geometric parameters. This systematic error limits the achievable positioning accuracy of the robot essentially. Only a few publications where flexibilities of the robot in the calibration are considered exist, see Whitney et al. (1986), Gong et al. (2000) or Khalil and Besnard (2002). In the paper Whitney et al. (1986) similar to our contribution a two stage method is proposed. They first identified a compliance model by performing multiple experiments with different external forces and then secondly the geometric calibration is performed by including displace-

ments according to the identified model from stage one. The papers of Gong et al. (2000) and Khalil and Besnard (2002) include the elastic displacements in the calculation of the geometric parameters but assumed that the stiffness is known. The goal of this contribution is to present a procedure, which in the first stage identifies the main flexibilities of our robot without external hardware. To this end, the methods presented in Hardeman (2008) and Wernholt (2007) are implemented which both performed frequency domain identifications of industrial robots. In the second stage, the elastic deflections are considered in the geometric calibration leading to reliable geometric parameters.

In Sect. 2 the dynamic model of our 6-axis articulated robot with joint and drive elasticities is derived. Section 3 deals with the modeling of the geometric error parameters, like joint offsets, axes misalignment, length errors and gear backlash. Subsequently, in Sect. 4 the elasticity parameters are identified, using a frequency domain approach as in the work of Hardeman (2008) and Wernholt (2007). The identification of the robots frequency response matrix is presented,
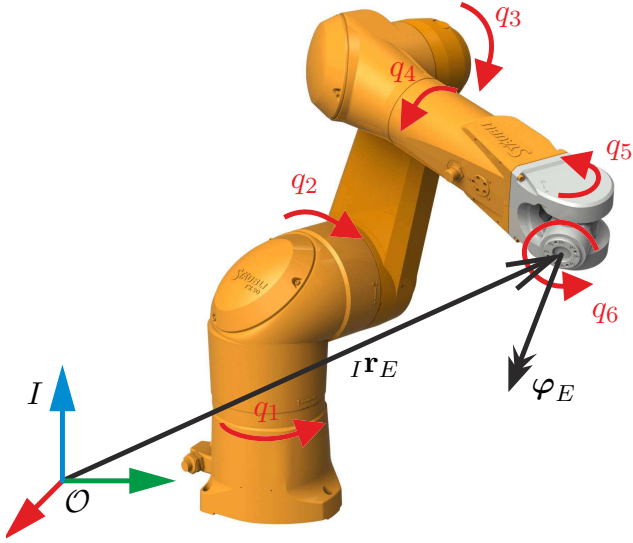
Figure 1. Arm coordinates of the Stäubli TX90L.

where the computation of suitable excitation signals are of prime importance. Then the matching between the transfer matrix of the dynamic model and the identified robot frequency response matrix is discussed. Finally in Sect. 5 the computation of the geometric parameters is addressed and the results for an industrial robot Stäubli TX90L are presented.

2 Dynamic modeling

This section deals with derivation of a dynamic model for the 6-axis industrial robot depicted in Fig. 1. Looking at the mechanical setup, the flexibilities of the first three joints and drives influence the positioning accuracy of the robots end-effector essentially. Hence, a finite bearing and drive stiffness is modeled leading to 4 degrees of freedom (DOF) for each axis $i = \{1, 2, 3\}$. The 4 DOF are composed of the motor position q_{iM}, the small bearing distortions q_{ix} and q_{iy} and the arm rotation q_i (see Fig. 2). The bearing distortions and the arm rotation are combined in the vector $\boldsymbol{q}_i^T = [q_{ix}, q_{iy}, q_i]$ representing the arm orientation. The modeling of flexible joints is motivated by the work of Hardeman (2008) which showed that the bearing and drive stiffness is at the same order of magnitude. Elastic effects of the last three axes (the spherical wrist) are of minor importance w.r.t. the end-effector positioning accuracy and are thus modeled without flexibilities. For the derivation of the dynamic model, the transformation from the body fixed frame of the previous arm (p) into the body fixed frame of the current arm (c) is necessary. Hence, the rotation matrix

$$\mathbf{R}_{\mathrm{cp}} = \mathbf{R}_\alpha|_{\alpha=q_{ix}} \, \mathbf{R}_\beta\big|_{\beta=q_{iy}} \, \mathbf{R}_\gamma\big|_{\gamma=q_i} \tag{1}$$

is introduced, where successive rotations about the main axes are performed. The rotation matrix for a rotation about the x, y or z axis is given by

$$\mathbf{R}_\alpha = \begin{bmatrix} 1 & 0 & 0 \\ 0 & \cos(\alpha) & \sin(\alpha) \\ 0 & -\sin(\alpha) & \cos(\alpha) \end{bmatrix},$$

$$\mathbf{R}_\beta = \begin{bmatrix} \cos(\beta) & 0 & -\sin(\beta) \\ 0 & 1 & 0 \\ \sin(\beta) & 0 & \cos(\beta) \end{bmatrix} \text{ or} \tag{2}$$

$$\mathbf{R}_\gamma = \begin{bmatrix} \cos(\gamma) & \sin(\gamma) & 0 \\ -\sin(\gamma) & \cos(\gamma) & 0 \\ 0 & 0 & 1 \end{bmatrix}, \tag{3}$$

respectively. The modeling is based on the paper of Öhr et al. (2006) where consecutive rotations are suggested to model joint and drive compliance. In total, the robot is represented by the vector $\boldsymbol{q}^T = [\boldsymbol{q}_{\mathrm{M}}^T, \boldsymbol{q}_{\mathrm{A}}^T, \boldsymbol{q}_{\mathrm{SW}}^T]$ consisting of the motor coordinates $\boldsymbol{q}_{\mathrm{M}}^T = [q_{1M}, q_{2M}, q_{3M}]$ the arm coordinates $\boldsymbol{q}_{\mathrm{A}}^T = [\boldsymbol{q}_1^T, \boldsymbol{q}_2^T, \boldsymbol{q}_3^T]$ and the coordinates of the spherical wrist $\boldsymbol{q}_{\mathrm{SW}}^T = [q_4, q_5, q_6]$. For the dynamic model, the bearing stiffness is modeled with linear springs and dampers c_{ix}, c_{iy} and d_{ix}, d_{iy} respectively and the drive stiffness and damping with the parameters c_i and d_i for axis $i = \{1, 2, 3\}$. For further details about the dynamical modeling see Öhr et al. (2006). Finally, the dynamic model is derived with the Projection Equation, see Bremer (2008) leading to the equation of motion

$$\mathbf{M}(\boldsymbol{q})\ddot{\boldsymbol{q}} + \boldsymbol{g}\left(\boldsymbol{q}, \dot{\boldsymbol{q}}, \boldsymbol{p}_{\mathrm{elast}}\right) = \mathbf{B}_{\mathrm{M}}\boldsymbol{\tau}_{\mathrm{M}} + \mathbf{B}_{\mathrm{SW}}\boldsymbol{\tau}_{\mathrm{SW}}$$

$$= \begin{bmatrix} \mathbf{I} \\ \mathbf{0} \\ \mathbf{0} \end{bmatrix} \boldsymbol{\tau}_{\mathrm{M}} + \begin{bmatrix} \mathbf{0} \\ \mathbf{0} \\ \mathbf{I} \end{bmatrix} \boldsymbol{\tau}_{\mathrm{SW}} \tag{4}$$

with the mass matrix $\mathbf{M}(\boldsymbol{q}) \in \mathbb{R}^{15 \times 15}$, the motor torques of the first three axis $\boldsymbol{\tau}_{\mathrm{M}} \in \mathbb{R}^{3 \times 1}$ and the motor torques of the spherical wrist $\boldsymbol{\tau}_{\mathrm{SW}} \in \mathbb{R}^{3 \times 1}$. Throughout the whole paper, the identity matrix is represented by $\mathbf{I}$ and the zero matrix/vector by $\mathbf{0}$. The vector $\boldsymbol{g}(\boldsymbol{q}, \dot{\boldsymbol{q}}, \boldsymbol{p}_{\mathrm{elast}})$ contains the Coriolis, centrifugal, gravitation and friction forces as well as the stiffness and damping parameters which are going to be identified and are combined in the vector

$$\boldsymbol{p}_{\mathrm{elast}}^T = [c_{1x}, c_{1y}, c_1, c_{2x}, c_{2y}, c_2, c_{3x}, c_{3y}, c_3, d_{1x}, d_{1y}, d_1,$$
$$d_{2x}, d_{2y}, d_2, d_{3x}, d_{3y}, d_3].$$

It is apparent from Eq. (4), that we are dealing with an underactuated system.

2.1 Linearized dynamic model

Basis for the calculation of the transfer matrix is the linearization of the dynamic model. A static equilibrium $\boldsymbol{q}_0$ ($\dot{\boldsymbol{q}}_0 = \mathbf{0}$, $\ddot{\boldsymbol{q}}_0 = \mathbf{0}$) is used as linearization point. The computation of the static equilibrium is presented in Sect. 2.3. For the
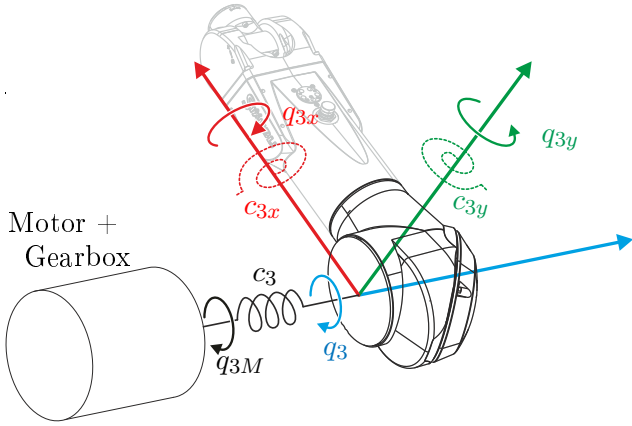
Figure 2. Model of the third axis.

linearization, a Taylor series expansion of Eq. (4) at the equilibrium configuration q_0 up to order 1 is carried out, leading to

$$\mathbf{M}_{\mathrm{lin}}\Delta\ddot{q} + \mathbf{D}_{\mathrm{lin}}\Delta\dot{q} + \mathbf{K}_{\mathrm{lin}}\Delta q = \mathbf{B}_{\mathrm{M}}\Delta\boldsymbol{\tau}_{\mathrm{M}} + \mathbf{B}_{\mathrm{SW}}\Delta\boldsymbol{\tau}_{\mathrm{SW}}$$
$$- \left(g\left(q_0, \mathbf{0}, p_{\mathrm{elast}}\right) - \mathbf{B}_{\mathrm{M}}\boldsymbol{\tau}_{\mathrm{M0}} - \mathbf{B}_{\mathrm{SW}}\boldsymbol{\tau}_{\mathrm{SW0}}\right) \quad (5)$$

with the mass matrix

$$\mathbf{M}_{\mathrm{lin}} = \mathbf{M}\left(q_0\right), \text{ the damping matrix } \mathbf{D}_{\mathrm{lin}} = \left.\frac{\partial g\left(q, \dot{q}, p_{\mathrm{elast}}\right)}{\partial \dot{q}}\right|_{q=q_0, \dot{q}=0},$$

the stiffness matrix $\mathbf{K}_{\mathrm{lin}} = \left.\dfrac{\partial \mathbf{M}(q)\ddot{q} + g\left(q, \dot{q}, p_{\mathrm{elast}}\right)}{\partial q}\right|_{q=q_0, \dot{q}=0, \ddot{q}=0}$

and $\boldsymbol{\tau}_{\mathrm{M}} = \boldsymbol{\tau}_{\mathrm{M0}} + \Delta\boldsymbol{\tau}_{\mathrm{M}}$ and $\boldsymbol{\tau}_{\mathrm{SW}} = \boldsymbol{\tau}_{\mathrm{SW0}} + \Delta\boldsymbol{\tau}_{\mathrm{SW}}$. The vectors $\boldsymbol{\tau}_{\mathrm{M0}}$ and $\boldsymbol{\tau}_{\mathrm{SW0}}$ represent the constant motor torques in the static configuration q_0. Thus, if q_0 is a valid static configuration the term $g(q_0, \mathbf{0}, p_{\mathrm{elast}}) - \mathbf{B}_{\mathrm{M}}\boldsymbol{\tau}_{\mathrm{M0}} - \mathbf{B}_{\mathrm{SW}}\boldsymbol{\tau}_{\mathrm{SW0}}$ vanishes, and we get the linearized equations of motion

$$\mathbf{M}_{\mathrm{lin}}\Delta\ddot{q} + \mathbf{D}_{\mathrm{lin}}\Delta\dot{q} + \mathbf{K}_{\mathrm{lin}}\Delta q = \mathbf{B}_{\mathrm{M}}\Delta\boldsymbol{\tau}_{\mathrm{M}} + \mathbf{B}_{\mathrm{SW}}\Delta\boldsymbol{\tau}_{\mathrm{SW}}. \quad (6)$$

2.2 Motor transfer matrix

For the identification of the modeled elasticity parameters, see Sect. 4, the transfer matrix from the motor torques $\boldsymbol{\tau}_{\mathrm{M}}$ to the motor accelerations $\ddot{q}_{\mathrm{M}}$ is necessary (Only the first three axes are included). By using the motor accelerations the double integrator behavior in the transfer matrix is avoided. Starting with the linearized robot dynamics of Eq. (6), the system is reduced to the coordinates q_{M} by using the selection matrix $\mathbf{F}_{\mathrm{M}}^T = [\mathbf{I}, \mathbf{0}]$ and the relation $\Delta q_{\mathrm{M}} = \mathbf{F}_{\mathrm{M}}^T \Delta q$. Using the principle of virtual work, we get the linearized motor equations

$$\mathbf{F}_{\mathrm{M}}^T\mathbf{M}_{\mathrm{lin}}\mathbf{F}_{\mathrm{M}}\Delta\ddot{q}_{\mathrm{M}} + \mathbf{F}_{\mathrm{M}}^T\mathbf{D}_{\mathrm{lin}}\mathbf{F}_{\mathrm{M}}\Delta\dot{q}_{\mathrm{M}} + \mathbf{F}_{\mathrm{M}}^T\mathbf{K}_{\mathrm{lin}}\mathbf{F}_{\mathrm{M}}\Delta q_{\mathrm{M}}$$
$$= \underbrace{\mathbf{F}_{\mathrm{M}}^T\mathbf{B}_{\mathrm{M}}}_{I}\Delta\boldsymbol{\tau}_{\mathrm{M}}. \quad (7)$$

The motor torques of the spherical wrist $\boldsymbol{\tau}_{\mathrm{SW}}$ vanish because $\mathbf{F}_{\mathrm{M}}^T\mathbf{B}_{\mathrm{SW}} = \mathbf{0}$. Applying the Laplace transformation to Eq. (7) we get

$$\mathbf{F}_{\mathrm{M}}^T\mathbf{M}_{\mathrm{lin}}\mathbf{F}_{\mathrm{M}}\Delta\bar{a}_{\mathrm{M}} + \mathbf{F}_{\mathrm{M}}^T\mathbf{D}_{\mathrm{lin}}\mathbf{F}_{\mathrm{M}}\Delta\bar{a}_{\mathrm{M}}\frac{1}{s}$$
$$+ \mathbf{F}_{\mathrm{M}}^T\mathbf{K}_{\mathrm{lin}}\mathbf{F}_{\mathrm{M}}\Delta\bar{a}_{\mathrm{M}}\frac{1}{s^2} = \Delta\bar{\boldsymbol{\tau}}_{\mathrm{M}} \quad (8)$$

with $\Delta a_{\mathrm{M}} = \Delta\ddot{q}_{\mathrm{M}}$. The vectors $\Delta\bar{a}_{\mathrm{M}}$ and $\Delta\bar{\boldsymbol{\tau}}_{\mathrm{M}}$ are the Laplace transformed values of Δa_{M} and $\Delta\boldsymbol{\tau}_{\mathrm{M}}$, respectively. Thus the transfer matrix leads to

$$\mathbf{G}^{[q_0]} = \Delta\bar{a}_{\mathrm{M}}\Delta\bar{\boldsymbol{\tau}}_{\mathrm{M}}^{-1} = \left(\mathbf{F}_{\mathrm{M}}^T\mathbf{M}_{\mathrm{lin}}\mathbf{F}_{\mathrm{M}}s^2 + \mathbf{F}_{\mathrm{M}}^T\mathbf{D}_{\mathrm{lin}}\mathbf{F}_{\mathrm{M}}s\right.$$
$$\left. + \mathbf{F}_{\mathrm{M}}^T\mathbf{K}_{\mathrm{lin}}\mathbf{F}_{\mathrm{M}}\right)^{-1}\mathbf{I}s^2 \quad (9)$$

where the superscript q_0 denotes the linearization point.

2.3 Determination of a static equilibrium

The calculation of a static equilibrium q_0 for our underactuated system, see Eq. (4) is neccessary for two different reasons. First, for the correct evaluation of the transfer matrix by using the correct linearization point, and second for the evaluation of the real robot pose and thus for the real endeffector position and orientation in a static configuration.

The motor position q_{M} and the coordinates of the spherical wrist q_{SW} are measured. Hence, only the static values of the arm coordinates q_{A} have to be computed. Therefore the linear system Eq. (5) is reduced to the coordinates of interest i.e. the arm coordinates q_{A}, by again applying the principal of virtual work and the relation $\Delta q_{\mathrm{A}} = \mathbf{F}_{\mathrm{A}}^T\Delta q$ with $\mathbf{F}_{\mathrm{A}}^T = [\mathbf{0}_{9\times3}, \mathbf{I}, \mathbf{0}_{9\times3}]$. Assuming a static solution – time derivatives of Δq are zero – we get

$$\mathbf{F}_{\mathrm{A}}^T\mathbf{K}_{\mathrm{lin}}\mathbf{F}_{\mathrm{A}}\Delta q_{\mathrm{A}} = \mathbf{F}_{\mathrm{A}}^T\mathbf{B}_{\mathrm{M}}\Delta\boldsymbol{\tau}_{\mathrm{M}} + \mathbf{F}_{\mathrm{A}}^T\mathbf{B}_{\mathrm{SW}}\Delta\boldsymbol{\tau}_{\mathrm{SW}}$$
$$- \mathbf{F}_{\mathrm{A}}^T\left(g\left(q_0, \mathbf{0}, p_{\mathrm{elast}}\right) - \mathbf{B}_{\mathrm{M}}\boldsymbol{\tau}_{\mathrm{M0}} - \mathbf{B}_{\mathrm{SW}}\boldsymbol{\tau}_{\mathrm{SW0}}\right). \quad (10)$$

Since the arm coordinates are not actuated $\mathbf{F}_{\mathrm{A}}^T\mathbf{B}_{\mathrm{M}} = \mathbf{F}_{\mathrm{A}}^T\mathbf{B}_{\mathrm{SW}} = \mathbf{0}$, Eq. (10) leads to

$$\mathbf{F}_{\mathrm{A}}^T\mathbf{K}_{\mathrm{lin}}\mathbf{F}_{\mathrm{A}}\Delta q_{\mathrm{A}} = -\mathbf{F}_{\mathrm{A}}^T g\left(q_0, \mathbf{0}, p_{\mathrm{elast}}\right). \quad (11)$$

If q_0 is a static pose of our robot, then $g(q_0, \mathbf{0}, p_{\mathrm{elast}}) = \mathbf{0}$ otherwise the displacement Δq_{A} is calculated by

$$\Delta q_{\mathrm{A}} = -\left(\mathbf{F}_{\mathrm{A}}^T\mathbf{K}_{\mathrm{lin}}\mathbf{F}_{\mathrm{A}}\right)^{-1}\mathbf{F}_{\mathrm{A}}^T g\left(q_0, \mathbf{0}, p_{\mathrm{elast}}\right) \quad (12)$$

according to Eq. (11). Thus the static solution q_0 can be calculated iteratively by

$$q_0^{(i+1)} = q_0^{(i)} + \mathbf{F}_{\mathrm{A}}\Delta q_{\mathrm{A}} \quad (13)$$

with the iteration index i. Because the stiffness of our robot is quite high, the initial solution

$$q_0^{(0)} = [q_{1M}, q_{2M}, q_{3M}, 0, 0, q_{1M}, 0, 0, q_{2M}, 0, 0,$$
$$q_{3M}, q_4, q_5, q_6]^T \qquad (14)$$

is obvious and often one iteration is sufficient to obtain a valid static solution. Having a valid static solution calculated, a geometric model is needed to evaluate the corresponding end-effector position and orientation.

3 Geometric model

The forward kinematics describes the end-effectors position $_Ir_E$ and orientation φ_E (see Fig. 1). Furthermore, it depends on the arm and wrist coordinates, q_A and q_{SW} respectively, and also on the geometric parameters. In this paper, the geometric parameters are separated into the known nominal values p_{nom} which describe the nominal kinematics of the robot and the unknown geometric error parameters p_{ge} comprising joint offsets, axes misalignment, length errors, and gear backlash. To model a joint offset p_0 for a rotation around the x axis with the DOF q the rotation matrix $\mathbf{R}$ leads to

$$\mathbf{R} = \mathbf{R}_\alpha |_{\alpha = q + p_0}. \qquad (15)$$

Axes misalignment, also for the example of a rotation around the x axis are introduced by adapting the rotation matrix $\mathbf{R}$ to

$$\mathbf{R} = \mathbf{R}_\alpha |_{\alpha = q} \mathbf{R}_\beta |_{\beta = p_\beta} \mathbf{R}_\gamma |_{\gamma = p_\gamma} \qquad (16)$$

with p_β and p_γ as misalignment angles. To include length errors the connection vector r which describes the links of our robot, is extended by the length error parameters p_{lx}, p_{ly} and p_{lz} leading to

$$r = \begin{bmatrix} l_x + p_{lx} \\ l_y + p_{ly} \\ l_z + p_{lz} \end{bmatrix}. \qquad (17)$$

Note, the parameters l_x, l_y and l_z are the nominal values of r. In contrast to the previous errors, gear backlash is not a geometric error and depend on the pose of the robot. In order to identify the direction in which the clearance is present, the center of mass of each body must be considered. To avoid the evaluation of the body dynamics the decision is based on the sign of the motor torque τ_M in each axis leading to the rotation matrix

$$\mathbf{R} = \mathbf{R}_\alpha |_{\alpha = q + \text{sign}(\tau_M) p_{BL}} \text{ with sign}(\tau_M) = \begin{cases} -1 & \tau_M < 0 \\ 0 & \tau_M = 0 \\ 1 & \tau_M > 0 \end{cases}. \qquad (18)$$

In the final geometric model of our robot, joint offsets, axes misalignments and length errors combined in the vector $p_i = [p_{0i}, p_{\beta i}, p_{\gamma i}, p_{lxi}, p_{lyi}, p_{lzi}]^T$ for all axes

$i = \{1, \ldots, 6\}$ as well as for the end-effector tool $i = E$ are included. Gear backlash p_{BLi} is only modeled for the second and third axes $i = \{2, 3\}$. The offset of the inertial frame of the robot and the external sensor (laser-tracker) is modeled by the length errors p_{lxI}, p_{lyI} and p_{lzI}. Thus finally, 47 error parameters combined in the vector $p_{ge} = [p_{lxI}, p_{lyI}, p_{lzI}, p_1^T, p_2^T, p_{BL2}, p_3^T, p_{BL3}, p_4^T, p_5^T, p_6^T, p_E^T]^T$ describe the end-effector position $_Ir_E(q_A, q_{SW}, p_{nom}, p_{ge})$ and orientation $\varphi_E(q_A, q_{SW}, p_{nom}, p_{ge})$ of the robot. Since the end-effector position and orientation depend on the arm coordinates, and the arm coordinates highly depend on the elasticity parameters their identification is treated in the next section.

4 Identification of elasticity parameters

For the identification of elasticity parameters, first the non-parametric frequency response matrix (FRM) see Pintelon and Schoukens (2012) of the real robot is determined, and second the transfer matrix calculated in Eq. (9) is adapted to the real one by adapting the elasticity parameters.

4.1 Identification of the non-parametric frequency response matrix

In standard operation mode, the robot is controlled by a feedback PD controller. To improve the identification accuracy, the influence of the PD controller is reduced by using small feedback gains. To ensure that the robot maintains the position, feed forward torque calculated from the inverse dynamics is added. The measurement setup is depicted in Fig. 3. The system is excited with periodic motor torques while simultaneously the actual motor torque and motor position is measured. The obtained measurement data is then transformed into the frequency domain and used for the FRM calculation. To reduce the effects of stick-slip transitions a sine wave with an amplitude of 3° serves as reference signal q_{Md} for the position controller. For the excitation of the system, normalized random multisine signals are used which leads to a separation of the FRM in three parts

$$\mathbf{G}(j\omega_k) = \mathbf{G}_{BLA}(j\omega_k) + \mathbf{G}_S(j\omega_k) + \mathbf{N}_G(j\omega_k) \qquad (19)$$

with $\mathbf{G}_{BLA}(j\omega_k)$ the best linear approximation (BLA), $\mathbf{G}_S(j\omega_k)$ the stochastic nonlinear contributions and $\mathbf{N}_G(j\omega_k)$ the errors due to the output noise (see Pintelon and Schoukens, 2012). We are interested in $\mathbf{G}_{BLA}(j\omega_k)$ which is used for the identification of the elasticity parameters in Sect. 4.2.

4.1.1 Calculation of the FRM

Assuming an appropriate excitation of the system, the measured motor torques and motor positions can be transformed to the frequency domain using the fast Fourier transformation (FFT). Note a signal x is represented in the frequency
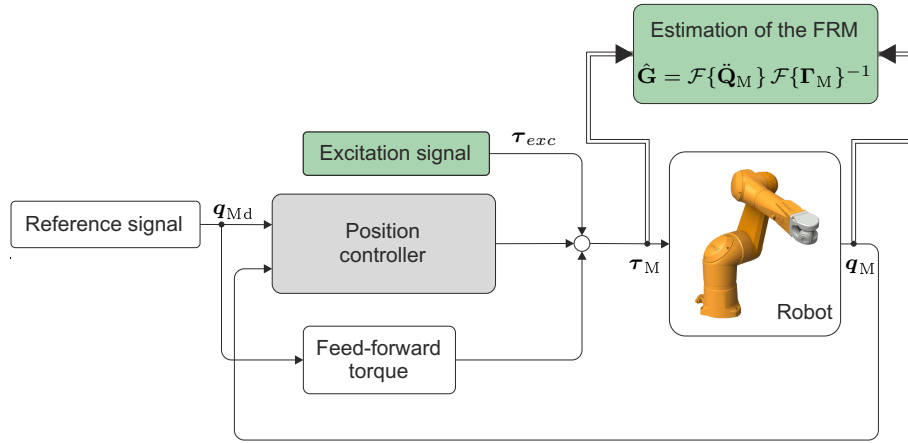
Figure 3. Block diagram of the control concept.

domain as $\overline{x}$ or $\mathcal{F}\{x\}$. In order to reduce the nonlinear contributions $\mathbf{G}_S$, N_r different excitation signals and to reduce the noise contribution $\mathbf{N}_G$, N_p periods are recorded. The FRM for an excitation signal r in pose q is calculated by

$$\hat{\mathbf{G}}^{[r,q]} = \mathcal{F}\{\ddot{\mathbf{Q}}_M\} \mathcal{F}\{\mathbf{\Gamma}_M\}^{-1} \qquad (20)$$

with $\ddot{\mathbf{Q}}_M = [\ddot{q}_{M,1} \, \ddot{q}_{M,2} \, \ddot{q}_{M,3}]$ and $\mathbf{\Gamma}_M = [\tau_{M,1} \, \tau_{M,2} \, \tau_{M,3}]$ resulting from measurement data for 3 orthogonal excitations, see Sect. 4.1.2. For different excitation signals, also slightly different FRM results are computed which have to be combined using averaging techniques. The choice of the averaging method depend on the signal to noise ratio (SNR) of the measurement data and the measurement setup. A comparison of different strategies is discussed in the paper of Wernholt and Moberg (2008). For our robot, the simple arithmetic averaging is useful, which is given by

$$\hat{\mathbf{G}}^{[q]} = \frac{1}{N_r} \sum_{r=1}^{N_r} \hat{\mathbf{G}}^{[r,q]}. \qquad (21)$$

4.1.2 Synthesis of the excitation signal

The quality of the FRM highly depends on the excitation signal. For frequency domain identification, periodic signals are very useful because they do not suffer from leakage effects. Furthermore the frequency resolution and power spectrum can be customized for the robot resulting in a minimum measurement time by a maximum quality of the signals (see Pintelon and Schoukens, 2012). Odd random phase multisine signals feature all these properties and are given by

$$\tau_{i,\text{exc}}(t) = \sum_{k=0}^{N_f-1} A_k \cos(\omega_k t + \phi_k), \, \omega_k = (2k+1)\omega_0,$$
$$\phi_k \in [0, 2\pi), \qquad (22)$$

consisting of N_f different frequencies of odd multiplicity of the basis frequency ω_0. We selected uniform distributed ran-

dom phases ϕ_k and a constant amplitude spectrum A_k. Because the FRM of the first three axes should be identified, a excitation signal for each motor has to be generated. Furthermore, for the FRM calculation with Eq. (20) the motor torque matrix $\mathbf{\Gamma}_M$ must have full rank. To get this property, three sets of orthogonal excitation signals are calculated. Therefore, three different odd random phase multisine signals according to Eq. (22) are generated and combined in a diagonal matrix leading to

$$\overline{\mathbf{D}}_R^{[r]}(k) = \begin{bmatrix} \overline{\tau}_{1,\text{exc}}(k) & 0 & 0 \\ 0 & \overline{\tau}_{2,\text{exc}}(k) & 0 \\ 0 & 0 & \overline{\tau}_{3,\text{exc}}(k) \end{bmatrix}. \qquad (23)$$

Matrix $\overline{\mathbf{D}}_R^{[r]}$ is generated in the frequency domain and k represents the discrete frequency index. The columns of $\overline{\mathbf{D}}_R^{[r]}(k)$ are orthogonalized using the matrix

$$T_{pq} = n_u^{-1/2} e^{j2\pi(p-1)(q-1)/n_u} \qquad (24)$$

with n_u the number of input signals ($n_u = 3$). This yields the excitation matrix

$$\mathbf{\Gamma}_{\text{exc}}^{[r]}(k) = \overline{\mathbf{D}}_R^{[r]}(k)\mathbf{T}. \qquad (25)$$

Each column of $\mathbf{\Gamma}_{\text{exc}}^{[r]}(k)$ represents one set of excitation signals and is orthogonal to the other ones. Using the matrix $\mathbf{T}$ in combination with the multisine signals $\overline{\mathbf{D}}_R^{[r]}(k)$ an arbitrary number of different but orthogonal excitation signals can be calculated.

4.1.3 Measurement procedure for the FRM identification

To calculate the FRM of our robot, N_r different excitation signals are calculated, each for N_p periods. Note, at least the first period of the measurement data can not be used for the FRM calculation because the system has to be in steady state. To reduce nonlinear contributions each excitation signal is
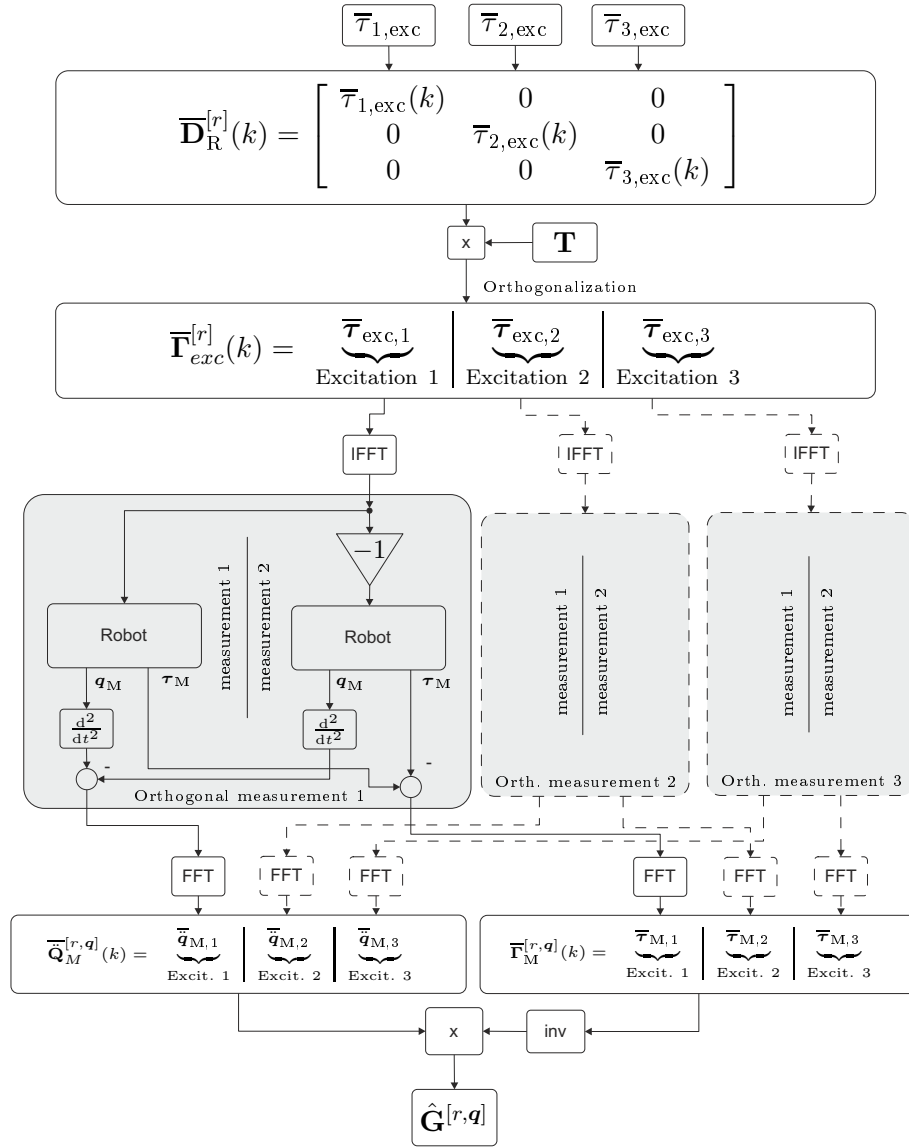
Figure 4. Measurement schedule for the FRM calculation of one realization.

applied once with positive and negative sign but with the same reference trajectory q_{Md}. Then the measurement data of these two excitations are subtracted from each other and are used for FRM calculation, as suggested in Hardeman (2008). Figure 4 shows a graphical representation of the procedure. It starts with the calculation of three independent excitation signals $\overline{\tau}_{i,\mathrm{exc}}$ using Eq. (22), and it ends with an accurate estimate of the FRM $\hat{\mathbf{G}}^{[r,q]}$ for one excitation r in pose q. The procedure is performed N_r times, leading to N_r slightly different FRM results which are in a next step averaged using Eq. (21). Our experiments have shown that $N_r = 4$ different realizations each with 4 periods, two periods for the calculation of the transfer matrix and two periods to get in steady state are convenient. The basis frequency of the excitation signal (see Eq. 22) is defined to $\omega_0 = 2\pi\,0.25\,\mathrm{rad\,s^{-1}}$. Hence

the signal has a period of 4 s. The excitation of the system for obtaining the transfer matrix for a single realization requires 96 s. This time is composed of the duration of the 3 orthogonal excitations (see Fig. 4) where each consists of a measurement with positive and negative sign with 4 periods. Thus all measurements (4 different realizations) are completed after 384 s. This yields $\hat{\mathbf{G}}^{[q]}$ which is shown in Fig. 5 for the pose $q\,P1$ of Fig. 6. To get a global representation of the robot, the FRM is identified in 3 different joint configurations. The selected poses are depicted in Fig. 6. These poses represent extrema regarding the moment of inertia in the considered axes. By using poses with extrema in the inertia, the obtained transfer matrices are assumed to be sufficiently different to identify global valid parameters. For all poses the FRM is
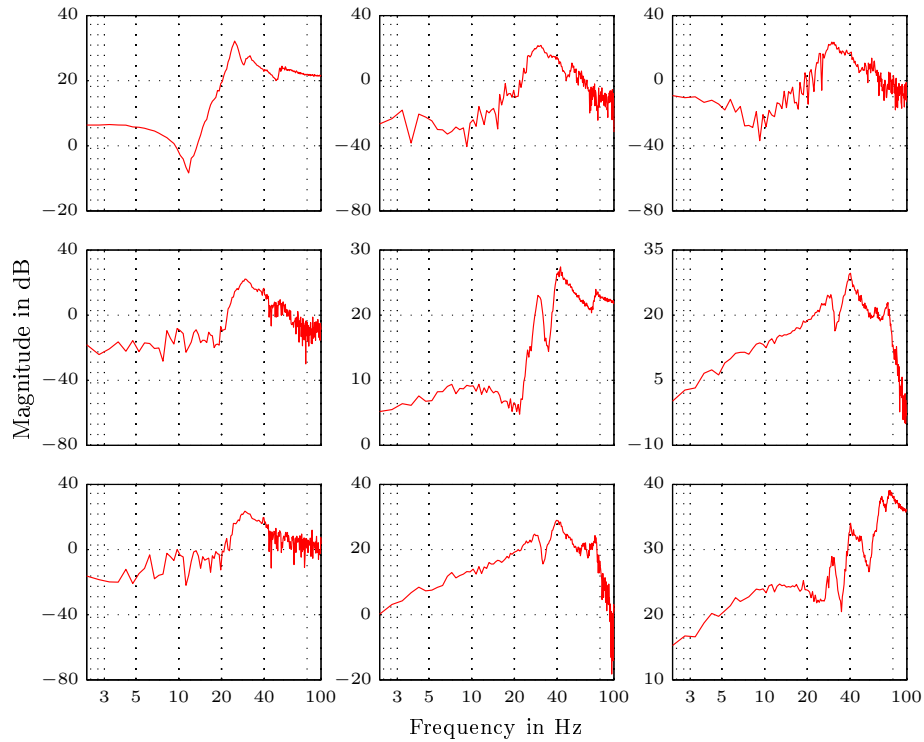
Figure 5. Calculated FRM $\hat{\mathbf{G}}^{[qP1]}$ with $N_{\mathrm{r}} = 4$.
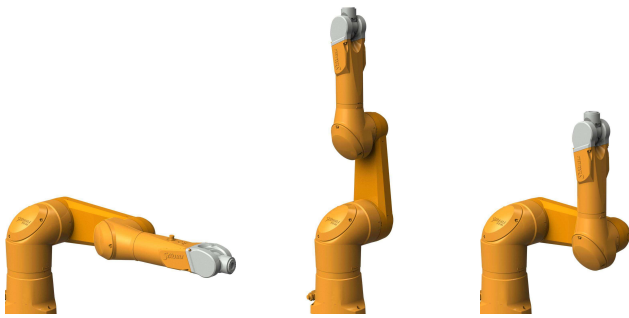
Figure 6. Poses for the FRM calculation represented by $qP1$, $qP2$ and $qP3$ from left to right respectively.

identified and used for the elasticity parameter identification of our robot.

4.2 Identification of the elasticity parameters

To identify the elasticity parameters, the parametric transfer matrix of our robot – derived in Sect. 2.1 and given by Eq. (9) – is fitted to the measured one, by changing the parameters $\boldsymbol{p}_{\mathrm{elast}}$. The fitting procedure performs a minimization of the cost functional

$$J\left(\boldsymbol{p}_{\mathrm{elast}}\right) = \sum_{\boldsymbol{q} \in \{qP1, qP2, qP3\}} \sum_{k=1\ldots N_\omega} \left[\boldsymbol{\Delta}^{[q]}\left(\omega_k, \boldsymbol{p}_{\mathrm{elast}}\right)\right]^*$$
$$\mathbf{W}^{[q]}\left(\omega_k\right)\left[\boldsymbol{\Delta}^{[q]}\left(\omega_k, \boldsymbol{p}_{\mathrm{elast}}\right)\right] \quad (26)$$

with the complex vector

$$\boldsymbol{\Delta}^{[q]}\left(\omega_k, \boldsymbol{p}_{\mathrm{elast}}\right) = \log\left(\mathrm{vec}\left(\hat{\mathbf{G}}^{[q]}\left(\omega_k\right)\right)\right)$$
$$- \log\left(\mathrm{vec}\left(\mathbf{G}^{[q]}\left(\omega_k, \boldsymbol{p}_{\mathrm{elast}}\right)\right)\right). \quad (27)$$

The minimization is carried out by applying a genetic algorithm followed by a gradient based minimization algorithm. The vector $\boldsymbol{\Delta}^{[q]}(\omega_k, \boldsymbol{p}_{\mathrm{elast}})$ represents the complex error between the measured FRM and the transfer matrix of the linearized system see Eq. (9). The superscript $*$ denotes the conjugate transpose matrix. To get a good fit in the region of interest, a weighting matrix $\mathbf{W}^{[q]}(\omega_k)$ is introduced. Especially the error in the vicinity of poles and zeros in the diagonal elements is amplified, leading to reasonable system parameters. Figure 7 shows both, the non-parametric FRM $\hat{\mathbf{G}}^{[qP1]}$ and the optimized parametric transfer function $\mathbf{G}^{[qP1]}$ in the first pose of the robot. It can be seen, that the coupling between the first and the other two axes is quite low and thus the measured and identified transfer functions agree not very well. Furthermore, the weighting matrix was tuned to get a good fit in the diagonal elements of the transfer matrices of poses $qP1$, $qP2$ and $qP3$. Figures 8 and 9 show the diagonal ele-
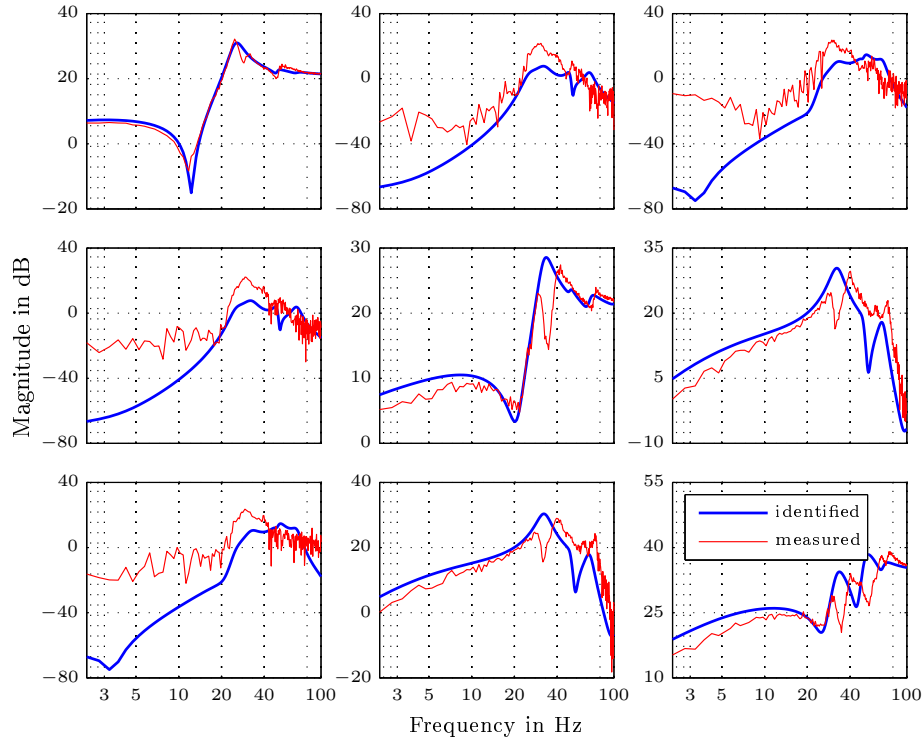
Figure 7. Comparison of the non-parametric FRM $\hat{\mathbf{G}}^{[qP1]}$ and the identified parametric one $\mathbf{G}^{[qP1]}$.
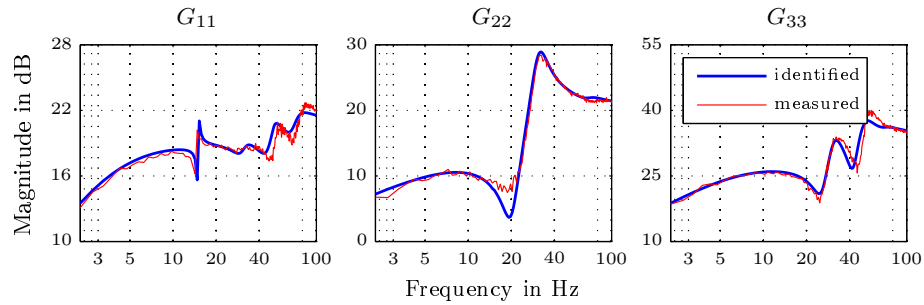
Figure 8. Comparison of the measured non-parametric FRM $\hat{\mathbf{G}}^{[qP2]}$ and the identified parametric one $\mathbf{G}^{[qP2]}$.

ments of the non-parametric and optimized parametric transfer matrices of the poses $qP2$ and $qP3$. Unfortunately, not all poles and zeros agree exactly, which is mainly attributed to nonlinearities in the stiffness parameters. Overall, a good fit between the non-parametric and parametric transfer functions is achieved and the identified parameters are listed in Table 1. Note, if only one pose is matched the accordance of the identified and measured FRM is very high but the parameters are not reliable anymore.

5   Geometric calibration

With the identified dynamic model of the last section the real robot pose due to the motor positions can be calculated. This estimated poses in combination with the real end-effector po-

sition, measured by an external sensor (laser-tracker), is used to calibrate the geometric model of Sect. 3. Our external sensor can not measure the end-effector orientation and thus the geometric calibration is discussed by using end-effector positions only.

5.1   Calculation of the estimated geometric parameters

The estimated end-effector position $_I r_E^{[q]}(q_A, q_{SW}, p_{nom}, p_{ge})$ can be evaluated by inserting the calculated arm coordinates q_A in Eq. (13) and the measured spherical wrist coordinates q_{SW}. Assuming small geometric errors we start with the initial vector of $p_{ge}^{(0)} = \mathbf{0}$. Thus the end-effector error for a set of N poses follows

Table 1. Identified elasticity parameters.

kNm rad^{-1}	kNm rad^{-1}	kNm rad^{-1}	kNms rad^{-1}	kNms rad^{-1}	kNms rad^{-1}
c_{1x}	c_{1y}	c_1	d_{1x}	d_{1y}	d_1
349.9	753.5	143.7	45.9	192.1	115.1
c_{2x}	c_{2y}	c_2	d_{2x}	d_{2y}	d_2
797.7	697.1	250.7	52.1	211.2	70.6
c_{3x}	c_{3y}	c_3	d_{3x}	d_{3y}	d_3
181.4	149.2	57.1	47.6	39.1	32.9
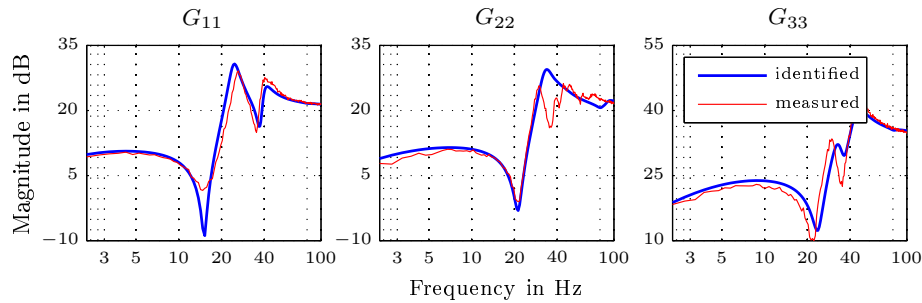
Figure 9. Comparison of the measured non-parametric FRM $\hat{\mathbf{G}}^{[qP3]}$ and the identified parametric one $\mathbf{G}^{[qP3]}$.

$$e_{\text{geo}} = \begin{bmatrix} {}_I \boldsymbol{r}_{\text{E,m}}^{[q1]} - {}_I \boldsymbol{r}_{\text{E}}^{[q1]} \\ \vdots \\ {}_I \boldsymbol{r}_{E,m}^{[qN]} - {}_I \boldsymbol{r}_E^{[qN]} \end{bmatrix} \qquad (28)$$

with ${}_I \boldsymbol{r}_{\text{E,m}}^{[q]}$ the end-effector position measured by the laser-tracker in pose $\boldsymbol{q}$ of the robot. Performing a Taylor series expansion on e_{geo} at $\boldsymbol{p}_{\text{ge}} = \boldsymbol{p}_{\text{ge}}^{(i)}$ of order 1 we get

$$e_{\text{geo,lin}} = \boldsymbol{\Theta} \Delta \boldsymbol{p}_{\text{ge}} + e_{\text{geo}}|_{\boldsymbol{p}_{\text{ge}}^{(i)}} \qquad (29)$$

with $\boldsymbol{\Theta} = \frac{\mathrm{d} e_{\text{geo}}}{\mathrm{d} \boldsymbol{p}_{\text{ge}}}|_{\boldsymbol{p}_{\text{ge}}^{(i)}}$. The superscript (i) indicates the current set of parameters. Unfortunately, not all geometric error parameters are independent, i.e. rank of $\boldsymbol{\Theta}$ is less than the number of parameters $\boldsymbol{p}_{\text{ge}}$. These linear dependencies must be eliminated. Therefore a numerical regularization algorithm which is based on a QR-decomposition is applied (see Gautier, 1991). 30 independent parameters out of the 47 modeled error parameters are found. The parameters $\boldsymbol{p}_{\text{ge}}$ are calculated by minimizing the error e_{geo}, using e.g. the Levenberg–Marquardt algorithm. The quality of the calibration result highly depends on the poses.

5.2 Calculation of optimal poses for the calibration

In order to get a good excitation of the geometric parameters the calibration poses are very important. In the paper of Sun and Hollerbach (2008a) the choice of the observability index for the pose calculation and in Sun and Hollerbach (2008b) and Zhuang (1994) selection algorithm for the computation

of optimal poses are presented. We used the algorithm presented in Sun and Hollerbach (2008b) where the minimum singular value of the covariance matrix $\boldsymbol{\Lambda} = \boldsymbol{\Theta}^T \boldsymbol{\Theta}$ is maximized. Finally, 40 optimal poses are calculated with a minimum singular value of $\sigma_{\min} = 0.46$. Exemplarily, 3 out of the 40 poses are depicted in Fig. 10. For all optimal poses the end-effector is measured with a laser tracker and the actual motor positions are measured by the motor encoders. Then, the estimated arm angles $\boldsymbol{q}_{\text{A}}$ are evaluated using Eq. (13) and the error of Eq. (28) is minimized using the Levenberg-Marquardt algorithm. The absolute positioning accuracy for the uncalibrated and calibrated case is depicted in Fig. 11. The positioning accuracy for the calibrated case is shown in Fig. 12. For the calibration poses, a positioning accuracy of about 0.1 mm is obtained which is in the range of the repeatability of our robot, and thus a very good result.

5.3 Evaluation of the absolute positioning accuracy

With the geometric parameters $\boldsymbol{p}_{\text{ge}}$ identified in the last section, the positioning accuracy in the whole workspace should be evaluated. Therefore 150 random poses in the whole workspace of the robot are generated and measurements with the laser-tracker. The calculated end-effector position due to the estimated robot configuration is compared to the measured position and the obtained absolute positioning accuracy is shown in Fig. 13. For 150 arbitrary poses an absolute error less than 0.32 mm and in 90 % of the poses an error less than 0.23 mm is obtained. If the elastic deflections are not considered in the calibration, the maximum error for the
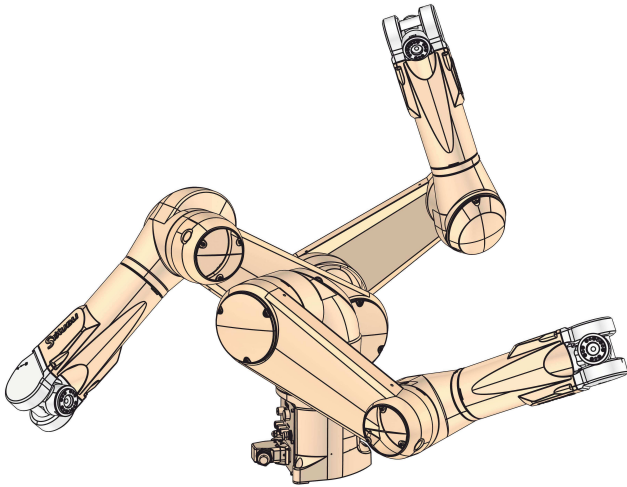
Figure 10. Three of the 40 optimal poses.
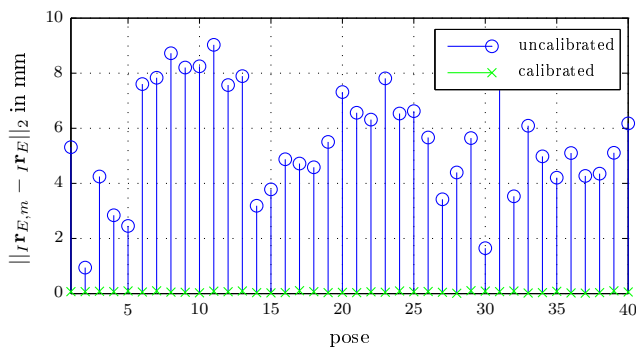
Figure 11. Absolute error of the end-effector for the calibration poses.

Figure 12. Error of the end-effector for the calibration poses in the inertial frame.
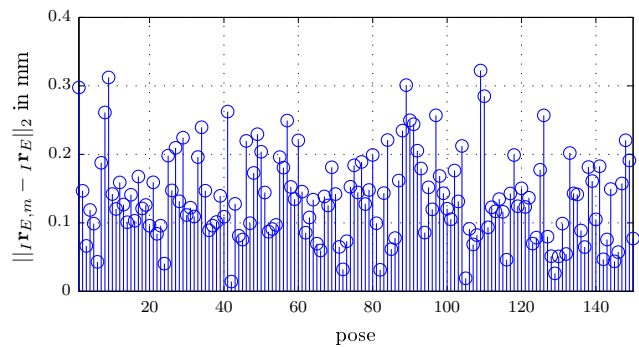
Figure 13. Absolute error of the end-effector for the 150 verification poses.

same poses is 0.7 mm which thus justifies the effort of the presented procedure.

6   Conclusions

This paper presents the identification of geometric parameters by including stiffness and damping parameters in the calibration process. Not only the inclusion of the elasticity parameters also their identification was discussed. The identification was carried out in the frequency domain, where the transfer matrix of the linearized system was adapted to the real robots transfer matrix by changing the elasticity parameters. Regarding the calculation of the real robots transfer matrix, the excitation signal is crucial and thus it is discussed in detail. The identification of globally valid parameters requires different poses. In this paper, the poses were selected manually. The calculation of optimal poses for the elasticity parameter identification is part of future work. With the identified elasticity parameters, the real robots configuration is estimated using the system dynamics and the geometric calibration is performed. Experimental results for a

Stäubli TX90L are reported. Thereupon geometric model parameters were identified which lead to a positioning accuracy of 0.32 mm in the whole workspace.

References

Bremer, H.: Elastic Multibody Dynamics: A Direct Ritz Approach, Springer Netherlands, 2008.

Gautier, M.: Numerical Calculation of Base Inertial Parameters of Robots, J. Robot. Syst., 8, 485–506, 1991.

Gong, C., Yuan, J., and Ni, J.: Nongeometric error identification and compensation for robotic system by inverse calibration, Int. J. Mach. Tools Manufact., 40, 2119–2137, 2000.

Hardeman, T.: Modeling and Identification of Industrial Robots Including Drive and Joint Flexibilities, PhD thesis, University of Twente, Twente, the Netherlands, 156 pp., 2008.

Khalil, W. and Besnard S.: Geometric Calibration of Robots with Flexible Joints and Links, J. Intell. Robot. Syst., 34, 357–379, 2002.

Khalil, W. and Dombre, E.: Modeling, Identification and Control of Robots, Kogan Page Science, London, UK, 2004.

Öhr, J., Moberg, S., Wernholt, E., Hanssen, S., Pettersson, J., Persson, S., and Sander-Tavallaey, S.: Identification of Flexibility Parameters of 6-axis Industrial Manipulator Models, in: Proceedings of ISMA2006, 18–20 September 2006, Leuven, Belgium, 3305–3314, 2006.

Pintelon, R. and Schoukens, J.: System Identification: A Frequency Domain Approach, John Wiley & Sons, Inc., Hoboken, New Jersey, 2012.

Siciliano, B. and Khatib, O.: Handbook of Robotics, Springer-Verlag, Berlin, Heidelberg, Germany, 2008.

Sun, Y. and Hollerbach, J. M.: Observability index selection for robot calibration, in: Proceedings on the IEEE International Conference on Robotics and Automation, 19–23 May 2008, Pasadena, USA, 831–836, 2008a.

Sun, Y. and Hollerbach, J. M.: Active robot calibration algorithm, in: Proceedings on the IEEE International Conference on Robotics and Automation, 19–23 May 2008, Pasadena, USA, 1276–1281, 2008b.

Wernholt, E.: Multivariable Frequency-Domain Identification of Industrial Robots, PhD thesis, Institute of Technology, University Linköping, Linköping, 204 pp., 2007.

Wernholt, E. and Moberg, S.: Experimental Comparison of Methods for Multivariable Frequency Response Function Estimation, in: Proceedings of the 17th IFAC World Congress, 6–11 July 2008, Coex, Korea, 15359–15366, 2008.

Whitney, D. E., Lozinski, C. A. and Rourke, J. M.: Industrial Robot Forward Calibration Method and Results, J. Dynam. Syst. Meas. Contr., 108, 1–8, 1986.

Zhuang, H.: Optimal selection of measurements configurations for robot calibration using simulated annealing, in: Proceedings on the IEEE International Conference on Robotics and Automation, 8–13 May 1994, San Diego, USA, 393–398, 1994.